The Astrophysical Journal, 945:95 (14pp), 2023 March 10 https://doi.org/10.3847/1538-4357/acb771
© 2023. The Author(s). Published by the American Astronomical Society.
OPEN ACCESS

# GRB 171205A: Hypernova and Newborn Neutron Star

Yu Wang[1,2,3], L. M. Becerra[2,4], C. L. Fryer[5,6,7,8,9], J. A. Rueda[1,2,10,11,12], and R. Ruffini[1,2,13]
[1] ICRA, Dipartimento di Fisica, Università di Roma "La Sapienza", Piazzale Aldo Moro 5, I-00185 Roma, Italy; yu.wang@inaf.it, laura.marcela.becerra@gmail.com, fryer@lanl.gov
[2] ICRANet, Piazza della Repubblica 10, I-65122 Pescara, Italy; jorge.rueda@icra.it
[3] INAF–Osservatorio Astronomico d'Abruzzo, Via M. Maggini snc, I-64100, Teramo, Italy; ruffini@icra.it
[4] Escuela de Física, Universidad Industrial de Santander, A.A.678, Bucaramanga, 680002, Colombia
[5] Center for Theoretical Astrophysics, Los Alamos National Laboratory, Los Alamos, NM, 87545, USA
[6] Computer, Computational, and Statistical Sciences Division, Los Alamos National Laboratory, Los Alamos, NM, 87545, USA
[7] The University of Arizona, Tucson, AZ 85721, USA
[8] Department of Physics and Astronomy, The University of New Mexico, Albuquerque, NM 87131, USA
[9] The George Washington University, Washington, DC 20052, USA
[10] ICRANet-Ferrara, Dipartimento di Fisica e Scienze della Terra, Università degli Studi di Ferrara, Via Saragat 1, I-44122 Ferrara, Italy
[11] Dipartimento di Fisica e Scienze della Terra, Università degli Studi di Ferrara, Via Saragat 1, I-44122 Ferrara, Italy
[12] INAF–Istituto di Astrofisica e Planetologia Spaziali, Via Fosso del Cavaliere 100, I-00133 Rome, Italy
[13] INAF, Viale del Parco Mellini 84, I-00136 Rome, Italy
*Received 2022 August 4; revised 2023 January 9; accepted 2023 January 29; published 2023 March 9*

## Abstract

GRB 171205A is a low-luminosity, long-duration gamma-ray burst (GRB) associated with SN 2017iuk, a broad-line type Ic supernova (SN). It is consistent with having been formed in the core collapse of a widely separated binary, which we have called the binary-driven hypernova of type III. The core collapse of the CO star forms a newborn NS ($\nu$NS) and the SN explosion. Fallback accretion transfers mass and angular momentum to the $\nu$NS, here assumed to be born non-rotating. The accretion energy injected into the expanding stellar layers powers the prompt emission. The multiwavelength power-law afterglow is explained by the synchrotron radiation of electrons in the SN ejecta, powered by energy injected by the spinning $\nu$NS. We calculate the amount of mass and angular momentum gained by the $\nu$NS, as well as the $\nu$NS rotational evolution. The $\nu$NS spins up to a period of 47 ms, then releases its rotational energy powering the synchrotron emission of the afterglow. The paucity of the $\nu$NS spin explains the low-luminosity characteristic and that the optical emission of the SN from the nickel radioactive decay outshines the optical emission from the synchrotron radiation. From the $\nu$NS evolution, we infer that the SN explosion had to occur at most 7.36 h before the GRB trigger. Therefore, for the first time, the analysis of the GRB data leads to the time of occurrence of the CO core collapse leading to the SN explosion and the electromagnetic emission of the GRB event.

*Unified Astronomy Thesaurus concepts:* Gamma-ray bursts (629); Neutron stars (1108); Pulsars (1306)

## 1. Introduction

The Burst Alert Telescope of the Neil Gehrels Swift Observatory on board (Swift-BAT) triggered and located GRB 171205A at 07:20:43 UT on 2017 December 17. Swift's X-Ray Telescope (XRT) began to observe 144.7 s after the BAT trigger (D'Elia et al. 2017). Soon, Izzo et al. (2017a) found that the burst was located in a nearby galaxy at redshift $z = 0.0368$, which was later confirmed by the X-shooter telescope on board the Very Large Telescope (VLT/X-shooter; Izzo et al. 2017b). About 5 days after, the associated type Ic supernova (SN) started to emerge and was detected by the 10.4 m Gran Telescopio Canarias (GTC; de Ugarte Postigo et al. 2017) and the SMARTS 1.3 m telescope (Cobb 2017).

This source has gained much observational attention since it was the third nearest gamma-ray burst (GRB) at the time of its discovery. D'Elia et al. (2018) performed a multiwavelength analysis of GRB 171205A using the data from the Swift and Konus-Wind satellites, covering from the optical to the sub-megaelectronvolt energies. Their cutoff power-law fit gives the peak energy at ∼100 keV and the isotropic energy in the order of $10^{49}$ erg, which implies this burst is a low-luminosity GRB and is an outlier of the Amati relation. Wang et al. (2018) reported the spectroscopic observation of the SN associated with the GRB, SN 2017iuk, and of the host galaxy. These observations showed that SN 2017iuk is a typical type Ic SN that resembles SN 2006aj, and that the host is an early-type, star-forming galaxy of high mass, low star formation rate, and low solar metallicity. In this source, for the first time, the polarization in the millimeter and radio bands during the afterglow phase was observed, thanks to the intensive combined use of the Submillimeter Array (SMA), the Atacama Large Millimeter/submillimeter Array (ALMA), and the Very Large Array (VLA), and showed a linear polarization <1% indicative of Faraday depolarization (Urata et al. 2019; Laskar et al. 2020). The observation continued for 1 yr, the ASKAP, ATCA, and $\mu$GMRT radio observations lasted ∼1000 days, the radio afterglow decays followed a shallow power law, and no jet break was exhibited (Maity & Chandra 2021; Leung et al. 2021). Figure 1 shows the multiwavelength light curve of GRB 171205A.

### 1.1. GRB 171205A in the Traditional Scenario

The origin of low-luminosity GRBs is still an open debate, and some interpretations include that these are bursts observed off-axis (Waxman 2004; Soderberg et al. 2006a, 2006b;

Original content from this work may be used under the terms of the Creative Commons Attribution 4.0 licence. Any further distribution of this work must maintain attribution to the author(s) and the title of the work, journal citation and DOI.

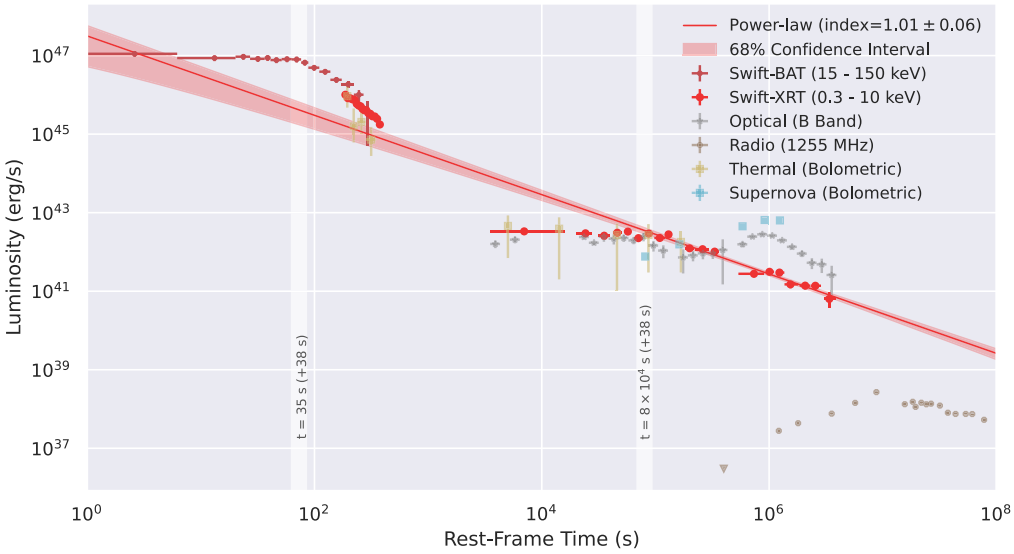


**Figure 1.** Luminosity light curve of Swift-BAT (deep red), Swift-XRT (red), optical $B$ band from D'Elia et al. (2018) (gray), and radio 1255 MHz from Maity & Chandra (2021) (brown), the triangles represent the upper limit. We also plot the thermal luminosity (yellow). The Swift-XRT data at time $>8 \times 10^4$ s is fitted by a power law index of $1.01 \pm 0.06$ and extrapolated to the earlier and the later time (red solid line, the red shadow represents the 68% confidence interval). Here, $T_0 = 0$ s is the starting time of the burst, corresponding to 38 s before the BAT trigger time.

Kathirgamaraju et al. 2016; Fraija et al. 2019a; Izzo et al. 2020), shock-wave breakout from the progenitor's shell (Campana et al. 2006; Li 2007; Soderberg et al. 2008; Barniol Duran et al. 2015; Irwin & Chevalier 2016; Fraija et al. 2019b), and emission from a jet-heated cocoon (Nakar 2015; Kasliwal et al. 2017; Gottlieb et al. 2018). GRB 171205A, as a low-luminosity GRB at a low redshift, provides a testing ground for the theoretical models. Izzo et al. (2019) found thermal X-ray and optical emissions radiated from material whose velocity evolves from $\sim 0.3c$–$0.1c$ in the first 7 days, and with a chemical composition that differs from that of SN 2017iuk, which has a lower velocity ($<0.1c$) evidenced by the spectroscopic analysis. They proposed the high-velocity material is a portion of the accelerated cocoon, which becomes transparent at $\sim$7 days, and then the SN dominates the optical emission. Suzuki & Maeda (2022) performed hydrodynamic simulations of a powerful jet penetrating the progenitor star and showed that jet-induced chemical mixing can lead to the observed chemical composition of the high-velocity material. Maity & Chandra (2021) analyzed GRB 171205A with the shock-wave breakout and the canonical off-axis jet models and show that both are inconsistent with the 1000 day observations. Compared to the observation, the shock-wave breakout model predicts a longer duration, a lower peak energy, and requires a higher column density. Moreover, the radius ($\sim 10^{13}$ cm) derived from the thermal component is too large for a typical progenitor. For the off-axis model, the discrepancies arise because the burst does not exhibit expected off-axis properties like a low peak energy, an increasing luminosity in the afterglow, and a frequency-independent break in the light curve (D'Elia et al. 2018). There are alternative models, e.g., Suzuki et al. (2019) modeled the burst as mildly relativistic spherical ejecta interacting with an ambient wind-like medium producing forward and reverse shocks and forming a thin shell. In their model, the prompt gamma-ray and X-ray emissions are produced when the optical depth of the shell reaches transparency, and subsequently, the radio and X-ray emissions are produced in the shock fronts by synchrotron and inverse Compton processes. They claimed this model can fit the prompt luminosity and duration, as well as the late-time X-ray, optical, and radio light curves.

### 1.2. The BdHN Scenario

Therefore, a satisfactory explanation of the multiwavelength data and the evolution with time of GRB 171205A remains an open issue. In this work, we analyze this source from the perspective of the binary-driven hypernova (BdHN) model of long GRBs. The progenitor of the GRB in the BdHN model is a binary system composed of a carbon-oxygen (CO) star and a neutron star (NS) companion. Numerical simulations of the sequence of physical processes occurring in a BdHN have been performed in the last decade and have led to a detailed picture and interpretation of the GRB observables (see, e.g., Izzo et al. 2012; Rueda & Ruffini 2012; Fryer et al. 2014; Becerra et al. 2015; Fryer et al. 2015; Becerra et al. 2016; Ruffini et al. 2018c; Becerra et al. 2019). The core collapse of the CO star leads to the formation of a newborn NS ($\nu$NS) at its center and ejects the outer layers of the star in an SN explosion. The ejecta accretes onto the NS companion and due to matter fallback there is also accretion onto the $\nu$NS (see, e.g., Wang et al. 2022; Becerra et al. 2022; Rueda et al. 2022b, and references therein). Both accretion processes are hypercritical (i.e., highly super-Eddington) in view of the activation of a very efficient neutrino emission (Becerra et al. 2016, 2018). For orbital periods of a few minutes, the NS companion reaches the critical mass for gravitational collapse, leading to a Kerr black hole (BH). These BdHN are referred to as type I (BdHN I). BdHN I explain the energetic GRBs with isotropic energies $\gtrsim 10^{52}$ erg. The accretion processes are observed as precursors of the prompt emission (see, e.g., Wang et al. 2019). The gravitomagnetic interaction of the newborn Kerr BH with the surrounding magnetic field induces an electric field. For a sufficiently supercritical magnetic field, the electric field becomes also supercritical leading to an electron–positron ($e^+e^-$) pair plasma. The self-acceleration of this plasma to Lorentz factors $\Gamma \sim 100$ and its transparency explain the ultrarelativistic prompt emission (UPE) phase (see Moradi et al. 2021b for the UPE analysis of

**Table 1**
Physical Phenomena that Occur in BdHN I–III, and their Associated Observables in the GRB Data

| Physical Phenomenon/Reference | BdHN Type | GRB Observable | | | | |
|---|---|---|---|---|---|---|
| | | $\nu$NS Rise (soft-hard X-rays) | UPE (MeV) | GeV emission | SXFs HXFs | Afterglow (X/optical/radio) |
| Early SN emission (a) | I, II, III | ⊗ | | | | |
| Hypercritical accretion onto $\nu$NS (b) | I, II, III | ⊗ | | | | |
| Hypercritical accretion onto NS (b) | I, II | ⊗ | | | | |
| BH formation from NS collapse (c) | I | | | ⊗ | | |
| Transparency of $e^+e^-$ (from vacuum polarization) with low baryon load region (d) | I | | ⊗ | | | |
| Synchrotron radiation inner engine: BH+$B$-field+SN ejecta (e) | I | | | ⊗ | | |
| Transparency of $e^+e^-$ (from vacuum polarization) with high baryon load (f) | I | | | | ⊗ | |
| Synchrotron emission from SN ejecta with energy injection from $\nu$NS (g) | I, II, III | | | | | ⊗ |
| Pulsar-like emission from $\nu$NS (g) | I, II, III | | | | | ⊗ |

**Note.** UPE stands for ultrarelativistic prompt emission, SXFs for soft X-ray flares, and HXFs for hard X-ray flares.
**References.** (a) Y. Aimuratov et al. (2023, in preparation), Wang et al. (2019, 2022), Rueda et al. (2022b), (b) Fryer et al. (2014), Becerra et al. (2016, 2022), Rueda et al. (2022b), Wang et al. (2022), (c) Ruffini et al. (2019), Moradi et al. (2021a, 2021b), (d) Bianco et al. (2001), Moradi et al. (2021b), Rastegarnia et al. (2022), (e) Ruffini et al. (2019), Rueda & Ruffini (2020), Moradi et al. (2021a), Rueda et al. (2022a), (f) Ruffini et al. (2018c), (g) Ruffini et al. (2018a), Wang et al. (2019), Rueda et al. (2020).

GRB 190114C, and Rastegarnia et al. 2022 for GRB 180720B). The electric field accelerates electrons to ultrarelativistic energies leading to synchrotron radiation, which explains the observed gigaelectronvolt emission (Ruffini et al. 2019; Rueda & Ruffini 2020; Moradi et al. 2021a; Rueda et al. 2022a). There is an additional synchrotron radiation process by relativistic electrons in the ejecta expanding in the $\nu$NS magnetic field. The $\nu$NS also injects energy into the ejecta. This synchrotron radiation explains the afterglow emission in the X-ray, optical, and radio wavelengths (see, e.g., Ruffini et al. 2018a; Wang et al. 2019; Rueda et al. 2020). Finally, the release of nickel decay (into cobalt) in the SN ejecta powers the bump observed in the optical in the late afterglow.

For longer orbital periods, of the order of tens of minutes, the NS companion does not reach the critical mass, so it remains a massive, fast-rotating NS. These BdHN are referred to as type II (BdHN II). BdHN II explain the less energetic GRBs with isotropic energies $\lesssim 10^{52}$ erg. The physical processes and related observables associated with the presence of the BH are clearly not observed in the BdHN II (e.g., the UPE and the gigaelectronvolt emission). The synchrotron afterglow in the X-ray, optical, and radio wavelengths, instead, is present both in BdHN I and II because it is powered by the $\nu$NS and the SN ejecta (see Wang et al. 2019, 2022 for GRB 180728A and GRB 190829A).

### *1.3. GRB 171205A and the Quest for BdHN III*

When considering BdHN with longer and longer orbital periods, possibly of hours, the effects associated with the presence of the binary companion become observationally irrelevant. Therefore, there is no GRB observable that can discriminate the presence or absence of a binary companion. Under the above circumstances, we model GRB 171205A neglecting the observational consequences of a companion NS. We shall refer to these low-luminous sources with energies $\lesssim 10^{49}$–$10^{50}$ erg as BdHNe III.

Table 1 summarizes the sequence of physical phenomena that occur in BdHN I–III, and their corresponding observables in the GRB data. Signatures from a binary companion appear only in BdHN I and II, while BdHN III shows only observables associated with the SN and the $\nu$NS.

In Section 2, we analyze the Swift observations and fit the time-resolved spectra using the Markov Chain Monte Carlo method, and then we generate the light curves for the prompt emission and afterglow, shown in Figures 1 and 2. The special feature of this burst is the presence of a thermal component in the early afterglow, where the temperature drops from about 90 to 70 eV in the first 300 s. In Section 3, we describe the physical process of this burst, we suggest that this low-luminosity burst originates from a strong SN (or a hypernova). The fallback accretion after the SN collapse heats up the SN ejecta, accelerating its outermost layer to mildly relativistic and the heated ejecta emits thermal radiation. This process is similar to the cocoon model, but the opening angle for the energy release of the fallback accretion is much larger than the traditional jet. This large opening angle is consistent with the absence of the jet break signal in the afterglow. Meanwhile, the fallback accretion spins up the central NS, which in turn injects energy to power the afterglow by losing its rotational energy. In Section 4, we establish the analytical solutions for the spin-up of the $\nu$NS due to the mass and angular momentum transfer during the accretion. We derive an analytical solution for the time required for the spin-up process using an accurate Padè approximant in the expression of the angular velocity as a function of time (see Figures 3 and 4). The spin period of the

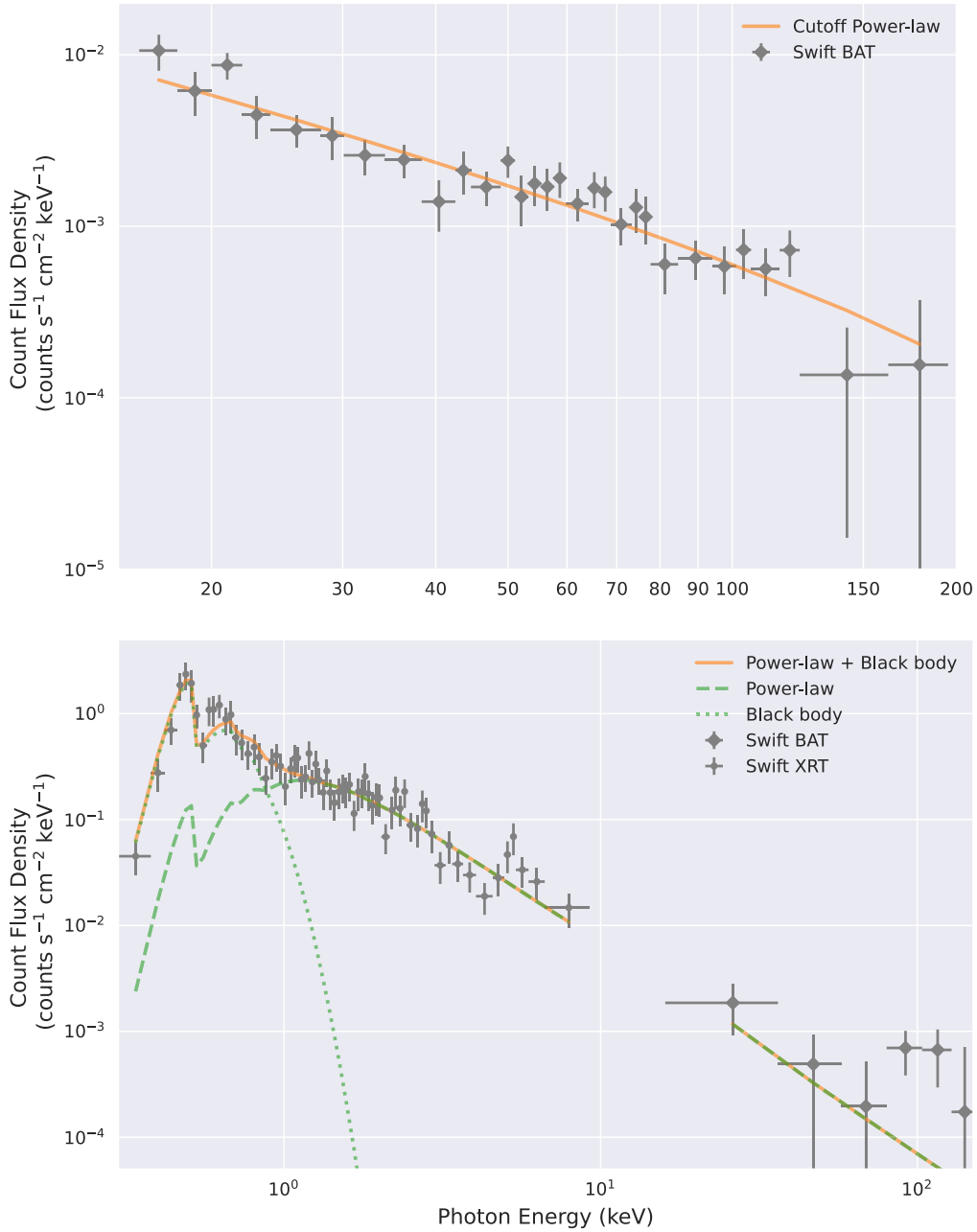


**Figure 2.** Top: spectrum of $T_{90}$ observed by BAT, fitted by a cutoff power-law model with a photon index of $\alpha = 1.10 \pm 0.35$ and peak energy $E_p = 148.55 \pm 121.97$ keV. Bottom: jointly spectral fitting of BAT and XRT from 151–162 s after the BAT trigger with a composite spectrum of a power law index of $\alpha = 2.00 \pm 0.17$ plus a blackbody of temperature $kT = 77.48 \pm 7.46$ eV.

NS required by the theory can be obtained from the observation by assuming that the energy of the X-ray afterglow is mainly contributed by the rotational energy of the $\nu$NS. From the observation of GRB 171205A, we derive that the $\nu$NS is possibly accelerated to a spin period of 47 ms, and 0.026 $M_\odot$ are accreted by the $\nu$NS via fallback. We show that this process takes 7.36 hr for a $\nu$NS born with zero spin. In Section 5, we present the model of the afterglow in the X-ray, optical, and radio wavelengths as originating from synchrotron radiation in the expanding SN ejecta with the energy injection from the central 47 ms spinning $\nu$NS pulsar. Section 6 shows the results of the fit of the X-ray, optical, and radio light curves with the above model (see Figure 5). Our conclusions are given in Section 7.

## 2. Spectrum and Light Curve

Swift-BAT and Swift-XRT data are retrieved from UKSSDC,[14] and the data reduction is performed by HEAsoft 6.29,[15] then the exported spectra are fitted by the Multi-Mission Maximum Likelihood framework (3ML; Vianello et al. 2015). In order to produce the luminosity light curve, the BAT data are binned following the thresholds that the signal-to-noise ratio is at least 6 and the maximal bin size is at most 50 s. Then each binned spectrum is fitted by a cutoff power-law function and is integrated from 15–150 keV according to the BAT bandwidth

[14] http://www.Swift.ac.uk
[15] http://heasarc.gsfc.nasa.gov/lheasoft/

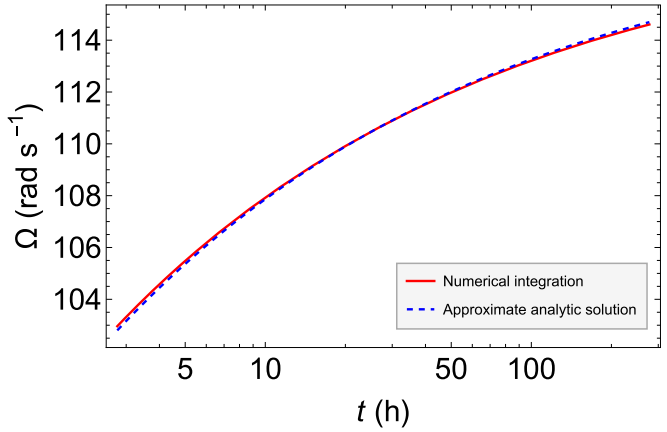


**Figure 3.** Comparison of the approximate solution of Equations (5) and (6) given by Equation (20), with the results from the full numerical integration, in the case $\mu(t_0) = 1.4$, $\Omega(t_0) = 0$, and $\chi = 0.15$.

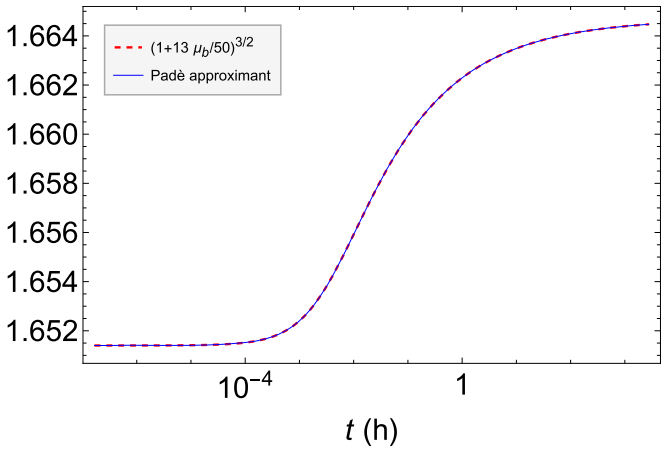


**Figure 4.** Comparison of the Padè approximant given by Equation (27) with the result of the full numerical integration.

to obtain the flux. After having the fitting parameters, the fluxes, and by adopting the FRW cosmology[16], the *k*-corrected luminosity light curve is obtained (Bloom et al. 2001). We generate the light curve of XRT in the energy range of 0.3–10 keV following a similar procedure, and the corresponding binning thresholds change to at least 200 counts and 10 s duration for the windows timing (WT) mode, as well as at least 100 counts and 100 s duration per bin for the photon counting mode. All the XRT spectra are fitted by a power-law function[17] with the photoelectric absorption models of our galaxy and the host galaxy. The generated Swift luminosity light curves are presented in Figure 1. We notice that this burst is seen since ∼38 s before the BAT trigger, hence, we set $T_0$ as 38 s before the BAT trigger time. The XRT light curve later than $8 \times 10^4$ s is fitted by a power-law function using lmfit (Newville et al. 2021), a python package for nonlinear optimization and curve fitting. lmfit implements the Levenberg–Marquardt method for optimization and is extended by numdifftool[18] to estimate the covariance matrix and then calculate parameter uncertainties. We obtain a power-law index of $1.01 \pm 0.06$ with the $1\sigma$ uncertainty (68% confidence level). We show the power-law fit in Figure 1 with the $1\sigma$ uncertainty region. The extrapolation of the power-law function coincides with the initial prompt luminosity.

The $T_{90}$ of the BAT observation lasts 189.19 s, and its time-integrated can be described by a cutoff power-law model with a power-law index of $\alpha = 1.10 \pm 0.35$, while the peak energy cannot be precisely constrained $E_p = 148.55 \pm 121.97$ keV. These parameters are consistent with those in D'Elia et al. (2018), which jointly fitted BAT and Konus-Wind data. They obtained $\alpha = 0.85^{+0.54}_{-0.41}$ and $E_p = 122^{+111}_{-32}$ keV, where the uncertainty of peak energy has been tightened because Konus-Wind covers higher energies than BAT. The integrated flux gives $(1.56 \pm 0.31) \times 10^{-8}$ erg cm$^{-2}$ s$^{-1}$ in the observed 15–150 keV bandwidth, and extrapolated to $(2.63 \pm 0.54) \times 10^{-8}$ erg cm$^{-2}$ s$^{-1}$ in 1–$10^4$ keV, which corresponds to the isotropic energy $E_{\rm iso} = (1.71 \pm 0.35) \times 10^{49}$ erg.

The presence of a thermal component in the afterglow of GRB 171205A has been reported in several articles (Campana et al. 2017; D'Elia et al. 2018; Izzo et al. 2019). Our time-resolved analysis also confirms that the additional thermal component significantly improves the fit to the low energy band of the XRT (<1 keV) until 324 s with a fitting blackbody temperature that drops from ∼90 to ∼70 eV, with an uncertainty of ∼10 eV. Afterward, the thermal spectrum gradually fades out of the XRT band (0.3–10 keV) as the temperature decreases. The WT data of XRT is unable to constrain the temperature at a times later than ∼4000 s, while the optical telescopes start to capture the thermal component that cools to the optical band (Izzo et al. 2019).

There is a common time window for BAT and XRT observing the source, from ∼151 s when XRT had slewed to the GRB position, until ∼162 s, the end of the $T_{90}$ of BAT. The BAT data at the end of the prompt emission is adequate to constrain the cutoff energy, hence, the model of a power law index of $\alpha = -2.00 \pm 0.17$ plus a blackbody component of $kT = 77.53 \pm 8.28$ eV is implemented to fit the entire data, as shown in Figure 2.

The optical and radio light curves shown in Figure 1 are reproduced from D'Elia et al. (2018) and Maity & Chandra (2021), respectively. The optical luminosity is unusually bright compared to the X-rays. Izzo et al. (2019) found that the evolution of the optical spectrum before and after 7 days is dominated by two black bodies with different evolution laws. The 1000 day radio light curve shows a shallow decay without any jet break signature. We refer to D'Elia et al. (2018), Izzo et al. (2019), Maity & Chandra (2021) for a detailed analysis and discussion of the optical and radio data, including the SN optical observation.

## 3. Physical Picture

At a given moment, a type Ic SN occurs from the core collapse of the CO star, forming at the same time a $\nu$NS at its center. The fallback accretion spins up the $\nu$NS (see Section 4), while releasing the accretion energy. From Becerra et al. (2019), the initial accretion rate is up to $10^{-3}\,M_\odot$ s$^{-1}$ and lasts

[16] The Friedman–Lemaître–Robertson–Walker metric is used for computing the luminosity distance, Hubble constant $H_0 = 67.4 \pm 0.5$ km s$^{-1}$ Mpc$^{-1}$, and matter density $\Omega_M = 0.315 \pm 0.007$ (Planck Collaboration et al. 2020).

[17] To have more data points for the light curve, our binning is more concerned with sufficiently short time resolution than with exact spectra. Therefore, the power-law model is used uniformly to fit the spectra, rather than the more accurate power-law plus blackbody model for which the data of each small bin cannot constrain all parameters. This introduces an error of less than 5%, which is in an acceptable level.

[18] https://numdifftools.readthedocs.io

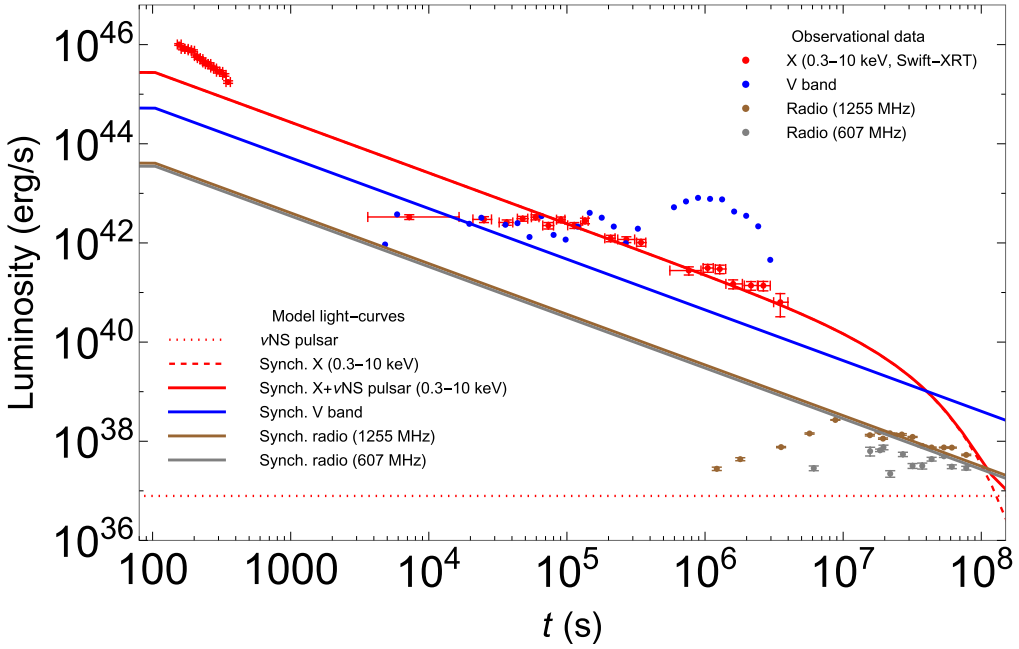


**Figure 5.** Luminosity of GRB 171205A in the X-ray (0.3–10 keV), optical (*V* band), and radio (607 MHZ and 1.255 GHz) energy bands compared with the luminosity predicted by the theoretical model. The rising part of the radio luminosity in the time interval of $10^6$–$10^7$ s is due to synchrotron self-absorption (see Maity & Chandra 2021, for details), here unmodeled. The X-ray data is retrieved from the Swift-XRT repository and analyzed in this article, and the optical and radio data are reproduced from D'Elia et al. (2018) and Maity & Chandra (2021).

tens of seconds, then it drops following a power law depending on the SN density profile. Therefore, in the initial phase of tens of seconds, the total energy generated from the accretion and to be injected into the stellar shells reaches $\sim 10^{52}$ erg, which is comparable to the kinetic energy of SN ejecta inferred from the optical emissions at a later time. Different from the traditional jetted model of GRBs, this amount of energy is emitted in a large opening angle of probably tens of degrees, it propagates in a portion of shells and accelerates the outermost shell to mildly relativistic velocity. The hydrodynamics can be referred to the simulation in Ruffini et al. (2018c), where has been simulated the propagation of GRB injected energy in the expanding stellar shells. The Lorentz factor of the shock wave is lower than 5 when it breaks out the outermost shell at $\sim 10^{12}$ cm. The acceleration of the accretion-powered blastwave is similar to that proposed for the shock-accelerated GRB model (Colgate 1974). In this scenario, a supernova blastwave accelerates as it propagates down the steep density gradient at the edge of a massive star (Colgate 1974; Tan et al. 2001). Although these models can produce highly relativistic ejecta in idealized conditions, the bulk of the material reaches only mildly relativistic velocities. Our model mirrors this evolution, differing only from this picture because the blastwave is propagating through an exploding CO star and is not spherical. Our asphericity has many of the features of the cocoon produced in jet models (see, e.g., Meszaros & Rees 2001; Ramirez-Ruiz et al. 2002; Zhang et al. 2004; Nakar & Piran 2017; Soker 2022; Eisenberg et al. 2022) that the jet pushes the stellar shells sideways to form a hot cocoon, a part of the cocoon emerges from the shells and expands outward with mildly relativistic velocity. Hence, both our picture and the cocoon picture involve some heated high-velocity material originating from the stellar shells expanding and emitting a thermal spectrum. The evolution of such this blackbody spectrum has been indeed observed by Swift-XRT and several optical telescopes, and a mass of $1.1 \times 10^{-3}\, M_\odot$ moving above $10^5$ km s$^{-1}$ has been inferred; see Figure 2 and Izzo et al. (2019). The difference is that in our picture, we expect a wider opening angle than in a jet, as we consider this low-luminosity GRB originates from a strong SN or hypernova in which the central compact object is the $\nu$NS. From the observations, there is no signature of any jet break in the afterglow until $\sim$1000 days (Maity & Chandra 2021; Leung et al. 2021), hence, preferring a large opening angle description.

At this stage, our system has three energy sources: the accretion, the spinning $\nu$NS, and the high-velocity material. For the prompt emission, this low-luminosity GRB deviates from the Amati relation (Amati et al. 2002); its peak energy ($E_p = 148.55$ keV, see Figure 2) is about one order of magnitude higher than the typical value of a weak GRB with isotropic energy $\sim 10^{49}$ erg (D'Elia et al. 2018). The deviation indicates this burst could be an extreme case or is formed by a different mechanism. Izzo et al. (2019) suggest that the jet deposits the majority of energy in the creation of the cocoon and only a small fraction of energy is emitted in gamma rays. In our framework, accretion dominates the energy release once the SN explodes, and the majority of energy is injected into the stellar shells, converting to the internal and kinetic energy of the SN ejecta, and producing the fast-moving material. The low isotropic energy of the prompt emission can be either produced by the tail of accretion or by the fast-moving material (De Colle et al. 2018). For the X-ray afterglow, it can be accounted for, at early times, by the synchrotron emission converted from the kinetic energy of the fast-moving material, and at times after the plateau, by the release of rotational energy of the $\nu$NS that has been spun up to periods of the order of milliseconds. We performed the numerical fitting of the spectrum and light curve using this scenario for several GRBs (see, e.g., Ruffini et al. 2018a; Wang et al. 2019; Rueda et al. 2020). This is also supported by that the ending time of the plateau coincides with

the transparency of the fast-moving material at $\sim 10^5$ s. For the optical afterglow, we share the same opinion as Izzo et al. (2019) that the fast-expanding mass dominates the optical emission before 4 days, then the dominance is overtaken by photons diffused out from the massive SN ejecta heated by the nickel radioactive decay.

The above picture contains many different physical processes, most of which have been discussed in detail and simulated, in the references mentioned in the text. However, after the birth of a $\nu$NS, the fallback accretion, the mass change, and the spin-up process have been rarely discussed in GRB studies. Hence, we will focus on modeling the properties of the $\nu$NS in the next section.

## 4. Spin-up and Fallback Accretion onto the $\nu$NS

We turn now to estimate the spin-up and the amount of mass that the $\nu$NS has accreted to gain enough rotational energy to power the X-ray afterglow emission, as specified in the BdHN model (see, e.g., Ruffini et al. 2021, for the analysis of 380 BdHNe).

Assuming the X-ray luminosity as a good proxy of the bolometric luminosity of the afterglow, we can estimate the change in the $\nu$NS rotational energy from a time $t_1$ to a time $t_2 > t_1$ from the energy balance equation, i.e.,

$$\int_{t_1}^{t_2} \dot{E}_{\rm rot}\, dt = E_{\rm rot}(t_2) - E_{\rm rot}(t_1) \approx -\int_{t_1}^{t_2} L_X dt. \tag{1}$$

After an infinite time, the $\nu$NS will have lost all its rotational energy; therefore, when $t_2 \to \infty$, we have $E_{{\rm rot},\infty}(t_2) \to 0$. So, assuming the time $t_1$ to be a generic time $t$, and the power-law luminosity

$$L_X = A_X t^{-\alpha_X}, \tag{2}$$

we obtain from Equation (1) that the $\nu$NS angular velocity evolves as

$$\Omega(t) \approx \sqrt{\frac{2A_X\, t^{1-\alpha_X}}{(\alpha_X - 1)I}}, \tag{3}$$

where $I$ is the stellar moment of inertia, which we have assumed constant with time, and can be estimated, for instance, using the EOS-independent approximate expression (Wei et al. 2019)

$$I \approx \left(\frac{G}{c^2}\right)^2 M^3 \sum_{i=1}^{4} \frac{b_i}{(M/M_\odot)^i}, \tag{4}$$

where $b_1 = 1.0334$, $b_2 = 30.7271$, $b_3 = -12.8839$, and $b_4 = 2.8841$.

In the case of GRB 171205A, the X-ray luminosity is fitted by a power law at times $t > t_{\rm pl} \approx 8 \times 10^4$ s, with $A_X = (3.165 \pm 0.238) \times 10^{47}$ erg s$^{-1}$, and $\alpha_X = 1.022 \pm 0.055$. Using these values, we estimate from Equation (3) that the rotation period of the $\nu$NS at $t = t_{\rm pl}$ is $P(t_{\rm pl}) \approx 51.01$ ms. If we assume that the $\nu$NS is spinning down from the $\nu$NS rise, i.e., from $t = t_{\nu\rm NS} \approx 35$ s, but the emission from it is partially absorbed by the high-velocity material, which is opaque before $\sim 10^5$ s, then by extrapolating from $t = t_{\rm pl}$ backward in time to $t = t_{\nu\rm NS}$, we infer that at the $\nu$NS-rise time, the $\nu$NS rotation period was $P_{\nu\rm NS} \equiv P(t_{\nu\rm NS}) \approx 46.85$ ms, i.e., $\Omega(t_{\nu\rm NS}) = 134.11$ rad s$^{-1}$.

We now estimate the mass accreted by the $\nu$NS before the $\nu$NS rise to spin it up to the above rotation rate. The accretion rate onto the $\nu$NS, set by the amount of mass from the inner layers of the expanding matter that fall back onto the $\nu$NS and their infalling speed, proceeds at hypercritical rates (see, e.g., Fryer et al. 1996). The accretion process makes the $\nu$NS increase its mass energy and rotation rate from the transfer of baryonic mass and angular momentum. The evolution of the $\nu$NS gravitational mass and angular momentum can be calculated from (Becerra et al. 2019)

$$\dot{M} = \left(\frac{\partial M}{\partial M_b}\right)_J \dot{M}_b + \left(\frac{\partial M}{\partial J}\right)_{M_b} \dot{J}, \tag{5}$$

$$\dot{J} = \tau_{\rm acc}, \tag{6}$$

where $J = I\Omega$ is the angular momentum, $M$ is the gravitational mass, $M_b$ is the baryonic mass, $\dot{M}_b$ is the baryonic mass accretion rate, and $\tau_{\rm acc}$ is the accretion torque.

Equation (5) must be complemented with the expressions of the two partial derivatives. These relations can be calculated from the fitting formula of the NS binding energy obtained in Cipolletta et al. (2015)

$$\mu_b - \mu = \frac{13}{200}\mu^2\left(1 - \frac{1}{130}j^{1.7}\right), \tag{7}$$

where $j \equiv cJ/(GM_\odot^2)$ is the dimensionless angular momentum and $\mu = M/M_\odot$. From it, we readily obtain

$$\left(\frac{\partial \mu}{\partial \mu_b}\right)_j = \frac{1}{1 + \frac{13}{100}\mu\left(1 - \frac{1}{130}j^{1.7}\right)}, \tag{8}$$

$$\left(\frac{\partial \mu}{\partial j}\right)_{\mu_b} = \frac{\frac{1.7}{2000}\mu^2 j^{0.7}}{1 + \frac{13}{100}\mu\left(1 - \frac{1}{130}j^{1.7}\right)}. \tag{9}$$

The numerical simulations of BdHNe performed in Becerra et al. (2019) show that the material accreted by the $\nu$NS circularizes around it in a sort of Keplerian disk structure before being accreted. Therefore, we assume that the accreted matter exerts onto the $\nu$NS the torque

$$\tau_{\rm acc} = \chi\, l\, \dot{M}_b, \tag{10}$$

where $l$ is the specific (i.e., per unit mass) angular momentum of the innermost stable circular orbit around the $\nu$NS, and $\chi \leqslant 1$ is an efficiency parameter of angular momentum transfer. For the angular momentum of the last stable circular orbit, we use the approximate EOS-independent results presented in Cipolletta et al. (2017),

$$l = 2\sqrt{3}\frac{GM}{c}\left[1 \mp 0.107\left(\frac{j}{M/M_\odot}\right)^{0.85}\right]. \tag{11}$$

We can obtain an approximate, analytic solution to Equation (6). For this task, we use the following analytic formula that fits the numerical results of the fallback accretion rate calculated in Becerra et al. (2019, 2022),

$$\dot{M}_b \approx \dot{M}_0(1 + \bar{t})^{-p}, \tag{12}$$

where $\dot{M}_0 = 7.2 \times 10^{-4} M_\odot$ s$^{-1}$, $t_{\rm acc} = 12$ s, $p = 1.3$, and we have introduced the notation $\bar{t} = t/t_{\rm acc}$.

For the involved rotation rates ($j \sim 0.01$), the contribution of the rotation terms in Equations (7) and (11) is negligible, so we can retain only the first term in those equations. With this

assumption, and integrating Equation (12), we have

$$\mu_b = \mu_b(t_0) + \frac{\dot{M}_0 t_{\rm acc}}{p-1}[1-(1+\bar{t})^{1-p}], \tag{13}$$

$$\mu \approx \frac{100}{13}\left(\sqrt{1+\frac{13}{50}\mu_b}-1\right), \tag{14}$$

$$l \approx 2\sqrt{3}\frac{GM_\odot}{c}\mu, \tag{15}$$

where $\mu_b(t_0) \approx \mu_0 + (13/200)\mu_0^2$, $\mu_0 = M(t_0)/M_\odot$ is the initial $\nu$NS gravitational mass, and we have inverted Equation (7) to write the gravitational mass in terms of the baryonic mass. Equations (13) and (14) imply that in the limit $t \to \infty$ the baryonic mass and the gravitational mass approach a maximum value

$$\mu_{b,\max} = \mu_b(t_0) + \frac{\dot{M}_0 t_{\rm acc}}{p-1} = \mu_b(t_0) + 0.0288, \tag{16}$$

$$\mu_{\max} = \frac{100}{13}\left(\sqrt{1+\frac{13}{50}\mu_{b,\max}}-1\right). \tag{17}$$

We now approximate the angular momentum derivative as $\dot{J} \approx I\dot{\Omega} \approx I_{\max}\dot{\Omega}$, where $I_{\max} = I(\mu_{\max})$, so that Equation (6) becomes

$$\dot{\Omega} \approx \beta\mu(t)(1+\bar{t})^{-p}, \quad \beta = \frac{2\sqrt{3}GM_\odot^2\chi\dot{\mu}_0}{cI_{\max}}, \tag{18}$$

whose solution can be written as

$$\Omega(t) = \Omega(t_0) + \beta\int_{t_0}^{t}\mu(t)(1+\bar{t})^{-p}dt. \tag{19}$$

Making the change in variable $x = (1+\bar{t})^{1-p}$, the integration of Equation (19) is straightforward leading to

$$\Delta\Omega = \Omega(t) - \Omega(t_0) = \omega\left\{x + \frac{2}{3}k\left[\left(1+\frac{13\mu_b}{50}\right)^{3/2} - \alpha^{3/2}\right] - 1\right\}, \tag{20}$$

where we have defined

$$\omega = \frac{100}{13}\frac{\beta\, t_{\rm acc}}{p-1}, \quad \Delta\mu_b = \frac{\dot{M}_0 t_{\rm acc}}{p-1} = 0.0288, \tag{21}$$

$$k = \frac{50}{13}\frac{1}{\Delta\mu_b} = 133.547, \quad \alpha = 1 + \frac{13}{50}\mu_{b,0} \tag{22}$$

and we have set the initial time $t_0 = 0$ since the fallback accretion begins soon after the SN explosion (see, e.g., Becerra et al. 2019). Figure 3 compares the approximate analytic solution (20) with the solution from the full numerical integration of Equations (5) and (6), in the case of $\mu(t_0) = 1.4$, $\Omega(t_0) = 0$, and $\chi = 0.15$.

Equation (20) tells us that in the limit $t \to \infty$ ($x \to 0$), the $\nu$NS reaches asymptotically a maximum angular velocity gain of

$$\Delta\Omega_{\max} = \omega\left\{\frac{2}{3}k\left[\left(1+\frac{13\mu_{b,\max}}{50}\right)^{3/2} - \alpha^{3/2}\right] - 1\right\}, \tag{23}$$

which as expected is larger for larger values of the angular momentum transfer efficiency parameter, $\chi$. Since we assume that after the $\nu$NS rise the $\nu$NS is spinning down, we seek solutions with a spinning up phase that ends with an angular velocity approaching the value that we have inferred at the $\nu$NS rise, i.e.,

$$\Omega_{\max} \approx \Omega(t_{\nu\rm NS}), \tag{24}$$

where $\Omega_{\max} = \Delta\Omega_{\max} + \Omega(t_0)$. We have used the approximate symbol in Equation (24) because by definition the value $\Omega_{\max}$ is reached only asymptotically. For practical purposes, we seek solutions in which $\Omega(t_{\nu\rm NS}) = 0.9\,\Omega_{\max}$. Therefore, given the values of $M$ and $\Omega(t_{\nu NS})$, the above constraint leads to a specific value of $\chi$ that leads to the self-consistent spin-up phase. For instance, for a $\nu$NS mass $M = 1.4M_\odot$ and

$$\Omega_{\nu\rm NS} \equiv \Omega(t_{\nu\rm NS}) = \sqrt{\frac{2A_X\, t_{\nu\rm NS}^{1-\alpha_X}}{(\alpha_X-1)I}} \approx 134.11 \text{ rad s}^{-1}, \tag{25}$$

we obtain $\chi = 0.182$.

We can also obtain a simple analytic estimate of the mass accreted by assuming that during the spin-up phase, the accretion rate, the gravitational mass, and the moment of inertia are constant and have their maximum values. Under this assumption, Equations (6) and (10) lead to the accreted mass in a time $\Delta t$,

$$\Delta\mu_b \approx \frac{cI_{\max}\Delta\Omega}{2\sqrt{3}\chi GM_\odot^2\mu_{\max}}. \tag{26}$$

For the above parameters, Equation (26) gives $\Delta\mu_b \approx 0.02570$. This is very close to the value obtained from the full numerical integration, $\Delta\mu_b = 0.02592$, which represents an error of only 0.85%. The accuracy of Equation (26) resides in the fact that the fallback accretion rate decreases as a power law, see Equation (12), hence most of the baryonic mass is accreted in the first minutes of the evolution. This explains why the above value of the accreted mass is close to the maximum accreted mass given by Equation (16), i.e., $\Delta\mu_{b,\max} = 0.0288$.

We turn to obtain an analytic expression of the time interval $\Delta t$ elapsed since the beginning of the fallback accretion, up to the instant when the $\nu$NS reaches a given angular velocity, or a given angular velocity gain, $\Delta\Omega$. In principle, we can obtain it by inverting Equation (20). However, the equation is highly nonlinear, so to obtain a relatively simple expression for it we use an accurate Padè approximant for the quantity involving the baryonic mass, i.e.,

$$\left(1+\frac{13\mu_b}{50}\right)^{3/2} = b^{3/2}(\tilde{\alpha}+X)^{3/2} \approx b^{3/2}(\mathcal{F}+\tilde{\alpha}^{3/2}),$$
$$\mathcal{F} = \frac{6\tilde{\alpha}^{3/2}X}{4\tilde{\alpha}-X}, \tag{27}$$

where $b = 1/k = (13/50)\Delta\mu_{b,\max}$, $\tilde{\alpha} = \alpha/b$, and we have introduced the variable $X = 1-x$. For the same example in Figure 3, we show in Figure 4 the excellent performance of the Padè approximant (27), which approximates the expression with a tiny error of only $10^{-9}$.

Using the approximant (27), Equation (20) becomes a second-order polynomial in the variable $X$ whose solution is

straightforward, leading to the time interval:

$$\Delta t = t_{\rm acc}[(1 - X)^{\frac{1}{1-p}} - 1], \tag{28}$$

where

$$X = \frac{B + \sqrt{B^2 + 4C}}{2}, \tag{29}$$

$$B = 4\tilde{\alpha} - 4\tilde{\alpha}^{3/2}\sqrt{b} - \Delta\Omega/\omega, \tag{30}$$

$$C = 4\tilde{\alpha}\Delta\Omega/\omega. \tag{31}$$

The relevance of the above time interval is that it allows computation of the time elapsed to reach the angular velocity at the $\nu$NS rise, $\Omega(t_{\nu\rm NS})$. Since it is close to the maximum value reachable by the fallback accretion, that time interval gives an estimate of the time elapsed since the SN explosion (SN rise), $t_{\rm SN}$. For the present example, we obtain

$$t_{\rm SN} = \Delta t(\Delta\Omega) = \Delta t(\Omega_{\nu\rm NS}) \approx 7.36\ {\rm hr}, \tag{32}$$

where we have used $\Delta\Omega = \Omega_{\nu\rm NS} - \Omega(t_0) = 134.11\ {\rm rad\ s^{-1}}$, as given by Equation (25). The full numerical integration leads to 7.20 hr, which implies that Equation (28) estimates the time interval with an error of only 2.2%.

## 5. Synchrotron and Pulsar Emission

We turn now to the specific modeling of the multi-wavelength afterglow of GRB 171205A. In the present scenario, the nonthermal component of the afterglow originates from the synchrotron radiation in the SN ejecta. The SN ejecta gets energy injected from the $\nu$NS fallback accretion and the multipolar emissions. Numerical calculations of this model applied to the description of the afterglow of specific GRBs can be found in Ruffini et al. (2018a), Wang et al. (2019), and Rueda et al. (2020). An analytic treatment of the model has been presented in Rueda (2022), and Wang et al. (2022) have applied it to model the afterglow of GRB 180720B. Our afterglow model relies more on continuous energy injections than the traditional forward shock-wave model, which relies on the kinetic energy of the jet. And unlike the traditional model that only considers the injection of dipole emission as an additional energy source to explain the short-duration plateau (e.g., internal plateau) (Dai & Lu 1998a, 1998b; Zhang & Mészáros 2001; Metzger et al. 2011; Lehner et al. 2012; Chen et al. 2017; Li et al. 2018; Zhao et al. 2020), our modeling process takes into account the fallback accretion, the dipole, and quadrupole radiation, such that continuous energy injections produce the long-lasting afterglow. Here, we follow the latter to estimate for GRB 171205A the emission generated by the synchrotron mechanism in the X-ray, optical, and radio wavelengths, and the $\nu$NS pulsar emission.

### 5.1. Synchrotron Emission by the Expanding Ejecta

The distribution of radiating electrons per unit energy, $N(E, t)$, is obtained from the solution of the kinetic equation (Kardashev 1962)

$$\frac{\partial N(E,\,t)}{\partial t} = -\frac{\partial}{\partial E}[\dot{E}\,N(E,\,t)] + Q(E,\,t), \tag{33}$$

where $Q(E, t)$ is the number of injected electrons into the ejecta per unit time $t$, per unit energy $E$, and $\dot{E}$ is the electron energy loss rate.

Following Rueda (2022) and Wang et al. (2022), we adopt the solution to Equation (33) for a self-similar uniform expansion

$$N(E,\,t) \approx \begin{cases} \dfrac{q_0}{\beta B_{*,0}^2(\gamma-1)}\hat{t}^{\,2}E^{-(\gamma+1)}, & t < t_q \\ \dfrac{q_0(t_q/t_*)^k}{\beta B_{*,0}^2(\gamma-1)}\hat{t}^{\,2-k}E^{-(\gamma+1)}, & t_q < t < t_b, \end{cases} \tag{34}$$

where $E_b < E < E_{\rm max}$,

$$E_b = \frac{\hat{t}}{\mathcal{M}t_*}, \quad t_b = \mathcal{M}t_*^2E_{\rm max}. \tag{35}$$

The model parameters are defined as follows. The ejecta expands self-similarly with the radiating layer being $r = R_* = R_{*,0}\,\hat{t}$, $\hat{t} \equiv t/t_*$, $t_* = R_*/v_* = R_{*,0}/v_{*,0}$, $v_* = R_*(t)/t = v_{*,0}$, $B_*(t) = B_{*,0}R_{*,0}/r = B_{*,0}\hat{t}^{-1}$ is the magnetic field strength at $r = R_*$, $\mathcal{M} \equiv \beta B_{*,0}^2/2$, $\beta = 2e^4/(3m_e^4c^7)$. We assume the injection power-law distribution of $Q(E,\ t) = Q_0(t)E^{-\gamma}$ (Kardashev 1962; Pacini & Salvati 1973; Rybicki & Lightman 1979; Longair 2011), where $\gamma$ and $E_{\rm max}$ are parameters to be determined from the observational data, and $Q_0(t)$ can be related to the power released by the $\nu$NS and injected into the ejecta from $L_{\rm inj}(t) = L_0(1 + t/t_q)^{-k} = \int_0^{E_{\rm max}} E\,Q(E,\,t)dE$, so $Q_0(t) = q_0(1 + t/t_q)^{-k}$, where $q_0 \equiv (2 - \gamma)L_0/E_{\rm max}^{2-\gamma}$.

The bolometric synchrotron radiation power of a single electron is given by (see, e.g., Longair 2011)

$$P_{\rm syn}(E,\,t) = \beta B_*^2(t)E^2 \approx \frac{\beta}{\alpha}B_*\nu, \tag{36}$$

where in the last equality we have used the fact that most of the radiation is emitted at frequencies near the so-called critical frequency, $\nu_{\rm crit} = \alpha B_*E^2$, where $\alpha = 3e/(4\pi m_e^3c^5)$. By setting $N(E,\,t) = \eta\,\hat{t}^{\,l}E^{-p}$, so that with the constants $\eta$ , $l$, and $p$ obtained by comparing this expression with Equation (34), the synchrotron luminosity radiated at frequencies from $\nu_1$ to $\nu_2 > \nu_1$ can be written as

$$\begin{aligned} L_{\rm syn}(\nu_1,\,\nu_2;\,t) &= \int_{\nu_1}^{\nu_2} J_{\rm syn}(\nu,\,t)d\nu \approx \nu J_{\rm syn}(\nu,\,t), \\ &\approx \frac{\beta}{2}\alpha^{\frac{p-3}{2}}\eta B_{*,0}^{\frac{p+1}{2}}\hat{t}^{\frac{2l-n(p+1)}{2}}\nu^{\frac{3-p}{2}}, \end{aligned} \tag{37}$$

where $\nu_1 = \nu$, $\nu_2 = \nu + \Delta\nu$, $\Delta\nu$ is the bandwidth. Here, $J_{\rm syn}$ is the spectral density, which is given by $J_{\rm syn}(\nu,\,t)d\nu \approx P_{\rm syn}(\nu,\,t)N(E,\,t)dE$ (see, e.g., Longair 2011). In Equation (37), we have made the approximation $\Delta\nu/\nu \ll 1$ because of the power-law character of the spectral density. Despite the synchrotron radiation of a single electron being beamed along the velocity of the particle, here we consider an isotropic distribution of a large number of electrons with an isotropic distribution of pitch angles, hence, leading to an isotropic total synchrotron luminosity.

### 5.2. $\nu$NS Evolution and Pulsar Emission

The $\nu$NS is subjected to the angular momentum loss driven by the magnetic field braking. In the point dipole+quadrupole magnetic field model presented in Petri (2015), the total

magnetic torque is given by

$$\tau_{\rm mag} = \tau_{\rm dip} + \tau_{\rm quad}, \tag{38}$$

$$\tau_{\rm dip} = -\frac{2}{3}\frac{B_{\rm dip}^2 R^6 \Omega^3}{c^3}\sin^2\alpha, \tag{39}$$

$$\tau_{\rm quad} = -\frac{32}{135}\frac{B_{\rm quad}^2 R^8 \Omega^5}{c^5}\sin^2\theta_1(\cos^2\theta_2 + 10\sin^2\theta_2), \tag{40}$$

where $\alpha$ is the inclination angle of the magnetic dipole moment with respect to the rotation axis, and the angles $\theta_1$ and $\theta_2$ specify the geometry of the quadrupole field. The strength of the magnetic dipole field is $B_{\rm dip}$. The dipole pure axisymmetric mode ($m=0$) is set by $\alpha=0$, and the pure $m=1$ mode by $\alpha=\pi/2$. The strength of the quadrupole magnetic field is $B_{\rm quad}$. The quadrupole $m=0$ mode is set by $\theta_1=0$, the $m=1$ mode by $\theta_1=\pi/2$ and $\theta_2=0$, while the $m=2$ mode is set by $\theta_1=\theta_2=\pi/2$. For the fit of the data, we shall adopt the $m=1$ mode for the dipole while the quadrupole can range between the $m=1$ and $m=2$ modes. The existence of multipolar magnetic fields in the $\nu$NS is supported by some theories and observations (Mastrano et al. 2013; Tiengo et al. 2013; Rodríguez Castillo et al. 2016; Pons & Viganò 2019). Therefore, we can write the total magnetic torque (38) as

$$\tau_{\rm mag} = -\frac{2}{3}\frac{B_{\rm dip}^2 R^6 \Omega^3}{c^3}\left(1 + \xi^2\frac{16}{45}\frac{R^2\Omega^2}{c^2}\right), \tag{41}$$

where $\xi$ is the quadrupole-to-dipole magnetic field strength ratio is defined by

$$\xi \equiv \sqrt{\cos^2\theta_2 + 10\sin^2\theta_2}\,\frac{B_{\rm quad}}{B_{\rm dip}}, \tag{42}$$

and the spin-down luminosity as

$$L_{\rm sd} = \Omega\,|\tau_{\rm mag}| = \frac{2}{3}\frac{B_{\rm dip}^2 R^6 \Omega^4}{c^3}\left(1 + \xi^2\frac{16}{45}\frac{R^2\Omega^2}{c^2}\right). \tag{43}$$

The evolution of the $\nu$NS is obtained from the energy conservation equation

$$-(\dot{W} + \dot{T}) = L_{\rm tot} = L_{\rm inj} + L_{\rm sd}, \tag{44}$$

where $W$ and $T$ are, respectively, the $\nu$NS gravitational and rotational energy.

## 6. Results

The emission of GRB 171205A comprises thermal and nonthermal components. In Section 1.1, we recalled that Izzo et al. (2019) explain the thermal component up to $10^5$ s in the X-rays and in the optical due to the cooling of fast-moving material. Here we here address the nature of the nonthermal component once the material is transparent. Therefore, the present model of synchrotron radiation described in Section 5 aims to explain the data that shows a decreasing power-law luminosity in the different energy bands with similar power-law indexes.

Table 2 summarizes the values of the model parameters that fit the afterglow of GRB 171205A in the X-ray, optical, and radio energy bands, as shown in Figure 5, obtained according to the above guidelines and the fitting procedure outlined in the Appendix.

**Table 2**
Value of the Synchrotron Model Parameters that Fit the Multiwavelength Observational Data of GRB 1701205A as Shown in Figure 5

| Parameter | Value |
|---|---|
| $t_*$ ($10^4$ s) | $2.650 \pm 110.276$ |
| $B_{*,0}$ ($10^5$ G) | $3.774 \pm 157.021$ |
| $\gamma$ | $1.606 \pm 0.231$ |
| $E_{\rm max}$ ($10^4\ m_e c^2$) | 3.738 |
| $k$ | $1.219 \pm 0.170$ |
| $L_0$ ($10^{47}$ erg s$^{-1}$) | $1.011 \pm 0.801$ |
| $t_q$ (s) | 100.00 |
| $B_{\rm dip}$ ($10^{12}$ G) | 1.000 |
| $P_{\nu\rm NS}$ (ms) | $46.852 \pm 64.910$ |

In the X-rays, the model describes the decreasing power-law behavior at times $>10^5$ s, and in the radio at times $>10^7$ s. We do not model the rising part of the radio emission in the time interval of $10^6$–$10^7$ s, which is due to synchrotron self-absorption (see Maity & Chandra 2021, for details).

The first relevant feature to notice is that the afterglow luminosity fades with time with an approximate power law $t^{-1}$. This power law is shallower than in GRBs of higher luminosity in which $t^{-1.3}$ (see, e.g., GRB 130427A or GRB 190114C in Ruffini et al. 2018a; Rueda et al. 2020). The pulsar emission from magnetic braking predicts a luminosity with a sharper power law, in a pure magnetic dipole the luminosity falls as $t^{-2}$, and for a pure magnetic quadrupole as $t^{-3/2}$ (see equations of Section 5.2 and Ruffini et al. 2018a; Rueda et al. 2020). Therefore, models based on pulsar emission from magnetic braking alone (even including higher-order multipole fields) are unable to fit the afterglow luminosity of GRB 171205A. This is the first indication of the necessity of an additional mechanism, in this case, the synchrotron radiation. The second relevant feature is that the afterglow in the X-ray and radio bands shows a similar power-law index (see the red, gray, and brown data points), as expected from the synchrotron model.

The optical data shows, instead, a flat behavior followed by the bump that characterizes the peak of the SN emission powered by the decay of nickel in the ejecta (Arnett 1996; Izzo et al. 2019). Both the synchrotron radiation and the SN radioactive decay contribute to the optical emission, but in GRB 171205A the latter dominates over the former. This explains the deviation of the optical luminosity from the typical power-law behavior of synchrotron radiation. This feature is consistent with the BdHN III nature of the source. In fact, BdHN III are low-luminous sources in which the $\nu$NS is not a very fast rotator, so it injects less energy into the ejecta in comparison to BdHNe I (e.g., GRB 130427A, 180720B, or 190114C; see Ruffini et al. 2018a; Rueda et al. 2020) and BdHNe II (e.g., GRB 190829A; see Wang et al. 2022). Therefore, the synchrotron emission is not very luminous and the emergent optical SN outshines the optical synchrotron luminosity. Interestingly, this latter feature of the emergent optical SN emission is also fulfilled in the most general situation of BdHN I and BdHN II (Y. Aimuratov et al. 2023, in preparation). SN 2017iuk is similar to the SNe associated with high-luminous GRBs, indicating that the pre-SN progenitor (i.e., the CO star and an NS companion) leading to the $\nu$NS in its core-collapse event, is similar for all long GRBs irrespective of their energetics (Y. Aimuratov et al. 2023, in preparation).

In the X-rays, the synchrotron luminosity fades off after a few $10^6$ s, when $h\nu_{\rm crit}$ falls below a kiloelectronvolt. At later

times, the power-law behavior continues in the optical and radio bands. The pulsar emission is characterized by a plateau followed by a power-law decay (at times longer than the characteristic spin-down timescale). For a plateau luminosity comparable (but smaller) to the synchrotron power-law luminosity, the sum of the two contributions can lead to a luminosity with a less sharp power-law behavior than that of the pure synchrotron. The afterglow of GRB 171205A does not show any signs of a change in the power law of the synchrotron emission (see Figure 5), so we cannot constrain the magnetic field strength and structure. In Figure 5, we have adopted ≈47 ms as the initial rotation period of the $\nu$NS and a pure dipole field ($\xi = 0$) of $B_{\rm dip} = 10^{12}$ G to guide the eye of the reader. For magnetic fields $\gtrsim 5 \times 10^{13}$ G, the plateau luminosity of the pulsar emission contributes appreciably to the total X-ray luminosity affecting the goodness of the fit. Therefore, we can assume the above estimate as an upper limit to the dipole magnetic field. For the present synchrotron model parameters, X-ray data after times of a few $10^6$ s could help constrain the presence of the pulsar emission. A sanity check of the model is that the energy injected into the ejecta is $\sim 10^{49}$ erg, of the same order as the rotational energy of the $\nu$NS, for a moment of inertia of a few $10^{45}$ g cm$^2$.

## 7. Conclusions

In this article, we have interpreted GRB 171205A within the BdHN model of long GRBs. In particular, because of the low energy release of only a few $10^{49}$ erg, we have classified GRB 171205A as a BdHN III, systems with long orbital periods, perhaps of the order of hours, in which the NS companion does not play any role in the cataclysmic event. Most of these binaries are also expected to be disrupted by the SN explosion (Fryer et al. 2015; Ruffini et al. 2016, 2018b). Under these circumstances, the GRB event is explained by the sole activity of the $\nu$NS and its interaction with the SN ejecta.

Here, we have shown that GRB 171205A is a low-luminous GRB consistent with it having been produced in the core collapse of a single CO star that forms the $\nu$NS and the type Ic SN. There are several new results related to the sequence of physical phenomena occurring in this system and the related GRB observables:

1. The fallback accretion is initially of a few of $10^{-3}\,M_\odot$ s$^{-1}$ and lasts tens of seconds (Becerra et al. 2019, 2022). The accretion energy is $\sim 10^{52}$ erg, comparable to the kinetic energy of the SN ejecta. This energy is injected into the ejecta, propagates, and accelerates the outermost shell to the observed mildly relativistic velocity. The hydrodynamics is similar to the case of the expanding SN ejecta with the GRB energy injection presented in Ruffini et al. (2018c). The Lorentz factor of the shock wave is $\lesssim 5$ when it gets transparency at $\sim 10^{12}$ cm, and emits a thermal spectrum. This scenario explains the prompt emission of GRB 171205A. This is also similar to the cocoon scenario advanced for this source in Izzo et al. (2019). Both pictures predict the heating of stellar shells (in our case by the physical process of the fallback accretion originating from the SN explosion and in the other by the postulation of an unspecified jet) that get boosted to high velocity and emit a thermal spectrum. The associated blackbody emission has been indeed observed in GRB 171205A, and it has been inferred that $\approx 10^{-3}\,M_\odot$ of material expands at velocities above $10^5$ km s$^{-1}$ (see Izzo et al. 2019 and Figure 2). The main difference between the two models is that in our picture there is no jet. This solution seems favored since the associated jet break expected in the afterglow of jetted GRB models is not observed in the data up to the last observations at ∼1000 days (Maity & Chandra 2021; Leung et al. 2021).
2. Regarding the afterglow emission, we have first inferred from an energy conservation argument, that the $\nu$NS should have started to lose its rotational energy at $t = 35$ s after the GRB trigger, i.e., from what we call the $\nu$NS rise, with a rotation period of 47 ms.
3. We have shown that the afterglow of GRB 171205A cannot be explained by the sole pulsar emission of the $\nu$NS by magnetic braking, even including higher multipole fields (e.g., quadrupole).
4. The multiwavelength afterglow is explained by synchrotron radiation emitted by electrons in the expanding SN, which is further powered by energy injected by the $\nu$NS. We have calculated the synchrotron luminosity in the X-ray, optical, and radio wavelengths with an analytic treatment of the above physical situation. We have shown that the X-rays and the radio luminosities follow the expectation from the synchrotron model. The rising part of the radio luminosity in the time interval of $10^6$–$10^7$ s is due to synchrotron self-absorption (see Maity & Chandra 2021, for details). The observed optical luminosity shows a flat behavior followed by the bump of the optical SN powered by the energy release in the ejecta of the radioactive decay of nickel into cobalt. We have shown that the synchrotron luminosity in those optical wavelengths lies below the luminosity of the emergent SN optical emission. This implies that the observed optical emission contains the contribution of both the synchrotron radiation and the optical SN.
5. Another remarkable fact to be highlighted is that SN 2017iuk, an SN associated with the low-luminous GRB 171205A, a BdHN III, shows similar properties (e.g., peak luminosity and peak time) to the SNe associated with high-luminous GRBs (BdHN I and II). This suggests that the pre-SN progenitor (i.e., the CO star) is similar for all long GRBs, irrespective of their energetics (Y. Aimuratov et al. 2023, in preparation).
6. There is a corollary of the above result. In low-luminous GRBs, i.e., in BdHN III like GRB 171205A, the relatively slow rotation (47 ms period) of the $\nu$NS implies the lower amount of energy injected into the ejecta, hence, the low energetics of the associated synchrotron emission. Under these circumstances, the optical emission of the SN powered by the nickel radioactive decay is able to outshine the optical synchrotron luminosity.
7. We calculated the evolution of the $\nu$NS mass and angular momentum (assumed to be initially zero) during the fallback accretion process leading to its spinning up to the 47 ms rotation period. From this evolution, we have inferred that the SN explosion occurred at most 7.36 hr before the GRB trigger time. This sets an estimate of the time delay between the SN explosion and the electromagnetic emission of the GRB event, assuming a $\nu$NS born with zero spin.

We thank the Referee for comments and suggestions that helped us in the presentation of this article. L.M.B. is supported by the Vicerrectoría de Investigación y Extensión—Universidad Industrial de Santander Postdoctoral Fellowship Program No. 2022000293.

## Appendix
## Fitting Procedure

In this appendix, we describe how we set the value of the model parameters from the physical scenario and specific observables, including the attached uncertainties. The parameters to be specified are the index of the electron's energy injection, $\gamma$, the parameters defining the injected power $k$, $L_0$, and $t_q$, the maximum energy of the electrons, $E_{\rm max}$, the self-similar expansion timescale, $t_*$, the magnetic field at the initial time of reference of the expansion, $B_{*,0}$, and the $\nu$NS dipole magnetic field strength $B_{\rm dip}$. In Section 4, we have already fixed the $\nu$NS rotation period, $P_{\nu\rm NS}$. Our aim is to estimate the uncertainty in each parameter from the propagation of the $1\sigma$ uncertainty of the power-law fit of the X-ray and radio luminosities.

Equation (37) shows that the signature of the present synchrotron model is the power-law luminosity in the different bands with (ideally) the same power-law index. Therefore, we constrain the synchrotron model parameters using the observational data showing the above property. Figure 5 shows that the X-ray (0.3–10 keV) luminosity data behaves as a power law in the time interval of $t\approx(0.87\text{–}5)\times10^6$ s, and the radio (1255 MHz) data in the time interval $t\approx(2.92\text{–}8)\times10^7$ s. The two luminosities are fitted by

$$L_X = A_X\, t^{-\alpha_X}, \qquad L_r = A_r\, t^{-\alpha_r}, \tag{A1}$$

where $A_X=(3.165\pm0.238)\times10^{47}$ erg s$^{-1}$, $\alpha_X=1.022\pm0.055$, $A_r=(4.290\pm0.178)\times10^{42}$ erg s$^{-1}$, and $\alpha_r=0.616\pm0.081$. The uncertainties at $1\sigma$ level. To estimate the uncertainties in the value of the model parameters, derived from the above fit, we follow the standard theory of error propagation. For instance, given quantity $f$ that is a function of the independent variables $a_i$, i.e., $f(a_1, a_2,...,a_n)$, its uncertainty can be estimated as (see, e.g., Ku 1966)

$$\delta f = \sum_{i=1}^{n}\sqrt{\left|\frac{\partial f}{\partial a_i}\right|^2(\delta a_i)^2} \approx \sum_{i=1}^{n}\left|\frac{\partial f}{\partial a_i}\right|\delta a_i. \tag{A2}$$

Thus, the uncertainties of the luminosities given by the power-law fits, Equation (A1), at a time $t$, can be estimated by

$$\delta L_i \approx \left|\frac{\partial L_i}{\partial A_i}\right|\delta A_i + \left|\frac{\partial L_i}{\partial \alpha_i}\right|\delta\alpha_i = \frac{\delta A_i}{A_{i,c}} + |-\ln t|\,\delta\alpha_i, \qquad i = X,\, r, \tag{A3}$$

where $A_{X,c}=3.165\times10^{47}$ erg s$^{-1}$, $A_{r,c}=4.290\times10^{42}$ erg s$^{-1}$, $\delta A_X=0.238\times10^{47}$ erg s$^{-1}$, $\alpha_{X,c}=1.022$, $\alpha_{r,c}=0.616$, $\delta A_r=0.178\times10^{42}$ erg s$^{-1}$, $\delta\alpha_X=0.055$, and $\delta\alpha_r=0.081$.

We turn to the self-similar expansion timescale, $t_*$, for which we must set values for $R_{*,0}$ and $v_{*,0}$. For $v_{*,0}$, we chose a fiducial value according to numerical simulations of the SN explosion (see, e.g., Becerra et al. 2016, 2019), so we set $v_{*,0}=10^8$ cm s$^{-1}$ and there is no propagated uncertainty to calculate for. With the above, we set the expansion timescale and its attached uncertainty

$$t_* = \frac{R_{*,0}}{v_{*,0}}, \qquad \delta t_* = \frac{\delta R_{*,0}}{v_{*,0}}. \tag{A4}$$

According to our working assumption of uniform expansion, the inner radius and its uncertainty are

$$R_{*,0} = v_{*,0}\, t_{\rm SN}, \qquad \delta R_{*,0} = v_{*,0}\,\delta t_{\rm SN}, \tag{A5}$$

where $t_{\rm SN}$ is the time since the SN explosion given by Equations (28) and (32), and $\delta t_{\rm SN}$ its uncertainty. For the above expansion velocity $v_{*,0}$, and the time since the SN explosion estimated in Section 4, $t_{\rm SN}\approx2.650\times10^4$ s $\approx$7.36 hr, we have $R_{*,0}\approx2.65\times10^{12}$ cm and $t_*=t_{\rm SN}=2.65\times10^4$ s. The uncertainty attached to the time $t_{\rm SN}$ can be estimated as

$$\delta t_{\rm SN} = \left|\frac{\partial t_{\rm SN}}{\partial\Omega_{\nu\rm NS}}\right|\delta\Omega_{\nu\rm NS}, \qquad \frac{\partial t_{\rm SN}}{\partial\Omega_{\nu\rm NS}} = \frac{1}{\omega}\frac{4\tilde{\alpha}-X}{2X-B}\frac{t_{\rm acc}}{1-p}[(1-X)^{\frac{p}{1-p}}], \tag{A6}$$

where $X$ and $B$ are given by Equations (29) and (30), evaluated at the time $t=t_{\nu\rm NS}$ s, so $\Delta\Omega=\Omega_{\nu\rm NS}$. The uncertainty in estimating $\Omega_{\nu\rm NS}$ from Equation (25) is given by

$$\delta\Omega_{\nu\rm NS} = \left|\frac{\partial\Omega_{\nu\rm NS}}{\partial A_X}\right|\delta A_X + \left|\frac{\partial\Omega_{\nu\rm NS}}{\partial\alpha_X}\right|\delta\alpha_X,$$
$$\frac{\partial\Omega_{\nu\rm NS}}{\partial A_X} = \frac{\Omega_{\nu\rm NS}}{2A_X},$$
$$\frac{\partial\Omega_{\nu\rm NS}}{\partial\alpha_X} = -\frac{\Omega_{\nu\rm NS}}{2}\left(\frac{1}{\alpha_X-1}+\ln t_{\nu\rm NS}\right). \tag{A7}$$

For the present parameters, i.e., $t_{\nu\rm NS}=35$ s and $\Omega_{\nu\rm NS}=134.11$ rad s$^{-1}$, we obtain from Equation (A7), $\delta\Omega_{\nu\rm NS}\approx185.795$ rad s$^{-1}$, so an uncertainty in the rotation period, $\delta P_{\nu\rm NS}=|\partial P_{\nu\rm NS}/\partial\Omega_{\nu\rm NS}|\delta\Omega_{\nu\rm NS}=2\pi\delta\Omega_{\nu\rm NS}/\Omega^2_{\nu\rm NS}\approx64.910$ ms. Using the above in Equation (A6), we obtain $\delta t_{\rm SN}\approx110.276\times10^4$ s $\approx306.220$ hr. Thus, we get from Equation (A5), $\delta R_{*,0}\approx110.276\times10^{12}$ cm, and from Equation (A4), $\delta t_*=\delta t_{\rm SN}$.

At large distances from the $\nu$NS, we expect the toroidal component of the magnetic field to dominate, which decays with distance as $r^{-1}$ (see, e.g., Goldreich & Julian 1969). Assuming a toroidal field of the same order as the poloidal field near the $\nu$NS surface, its value at the radius $r=R_{*,0}$ is

$$B_{*,0} \approx B_{\rm dip}\frac{R}{R_{*,0}} = B_{\rm dip}\frac{R}{v_{*,0}t_*}, \tag{A8}$$

where $B_{\rm dip}$ is the strength of the dipole magnetic field and $R$ is the fiducial $\nu$NS radius. As discussed in Section 7 the data does not constrain the dipole field but only sets an approximate upper limit of $B_{\rm dip,max}\approx5\times10^{13}$ G. Therefore, we shall adopt a fiducial, conservative magnetic field value $B_{\rm dip}=10^{12}$ G. By using a fiducial $\nu$NS radius $R=10^6$ cm, and the value of $R_{*,0}$ given by Equation (A5), we obtain $B_{*,0}\approx3.774\times10^5$ G. With the choice, Equation (A8), the attached uncertainty is given by

$$\delta B_{*,0} = B_{*,0}\frac{\delta R_{*,0}}{R_{*,0}} = B_{*,0}\frac{\delta t_*}{t_*} = B_{*,0}\frac{\delta t_{\rm SN}}{t_{\rm SN}}, \tag{A9}$$

which leads to $\delta B_{*,0}\approx157.021\times10^5$ G.

We now set the index $\gamma$. From Equation (37), we infer that the ratio of the synchrotron luminosity at two frequencies, $\nu_1$ and $\nu_2$, is given by $L_{\rm syn}(\nu_1)/L_{\rm syn}(\nu_2) = (\nu_1/\nu_2)^{\frac{3-p}{2}}$, where $p = \gamma + 1$. Therefore, we can constrain the value of the index $\gamma$ using the data in the X-rays and in the radio as

$$\gamma = 2\left[1 - \frac{\ln(L_X/L_r)}{\ln(\nu_X/\nu_r)}\right], \tag{A10}$$

where $L_X$ and $L_r$ are given in Equation (A1). Since the fitted power laws are not equal, the value of $\gamma$ inferred from Equation (A10) depends on the time at which we calculate the ratio of the luminosities. Therefore, we adopt for $\gamma$ the value given by the mean $\langle\gamma\rangle = \Delta t^{-1}\int\gamma dt$. We obtained $\langle\gamma\rangle \approx 1.6060$, where we have used $\Delta t \approx 8\times10^7$ s, $\nu_X = 10\,{\rm keV}/h \approx 2.423\times10^{18}$ Hz, and $\nu_r = 1255$ MHz. From Equation (A10), the uncertainty in the choice of $\gamma$ can be estimated as

$$\begin{aligned}\delta\gamma &= \left|\frac{\partial\gamma}{\partial L_X}\right|\delta L_X + \left|\frac{\partial\gamma}{\partial L_r}\right|\delta L_r \\ &= \frac{2}{\ln(\nu_X/\nu_r)}\left(\frac{\delta L_X}{L_X} + \frac{\delta L_r}{L_r}\right),\end{aligned} \tag{A11}$$

whose mean for the above parameters is $\langle\delta\gamma\rangle = 0.231$.

The synchrotron emission peaks around the critical frequency

$$\nu_{\rm crit} = \alpha B_* E^2 = \alpha B_{*,0} E^2 \frac{t_*}{t}, \tag{A12}$$

and then cuts off exponentially, where $E$ is the electron energy. Since the critical frequency decreases with time, there is a hard-to-soft evolution of the cutoff and the X-ray data give the strongest constraint. The electrons of maximum energy, $E_{\rm max}$, produce the maximum critical frequency, $\nu_{\rm crit,max}$. By requiring that $\nu_{\rm crit,max} = \nu_X$ at a cutoff time $t_{\rm cut,X} > t_{f,X}$, where $t_{f,X} \approx 3.5\times10^6$ s is the time of the last observational X-ray data, we obtain that the maximum electron energy must at least have the value

$$E_{\rm max} = \sqrt{\frac{\nu_X\, t_{\rm cut,X}}{\alpha\, t_*\, B_{*,0}}} = \sqrt{\frac{\nu_X\, v_{*,0}\, t_{\rm cut,X}}{\alpha\, B_{\rm dip} R}}, \tag{A13}$$

where in the last equality we have used Equation (A8). The cutoff time must allow the power-law luminosity to extend at least up to $t_{f,X}$. Thus, we chose $t_{\rm cut,X}$ such that the exponential cutoff at the time $t = t_{f,X}$ has reduced the power-law X-ray luminosity to one part in a thousand. With this condition, we find $t_{\rm cut,X} \approx 2.418\times10^7$ s, so $E_{\rm max} = 3.738\times10^4 m_e c^2$. Equation (A13) tells us that $E_{\rm max}$, chosen in this way, depends only on fiducial values that we have set for $v_{*,0}$, $B_{\rm dip}$, $R$, and $t_{\rm cut,X}$, so we cannot estimate an attached uncertainty to it.

Having set all the above parameters, it remains to set the parameters of the injected power, $L_0$, $k$, and $t_q$. The synchrotron luminosity increases at times $t < t_q$ (see Section 5.1) and decreases at times $t > t_q$. The X-rays' luminosity always shows a decreasing behavior, so we set $t_q = 100$ s, which roughly corresponds to the initial time of the X-ray data. For the parameters $L_0$ and $k$, we equate the model synchrotron luminosity, Equation (37), in the case of X-rays with the power-law luminosity (A1). From this equality, we obtain

$$\begin{aligned}k &= \frac{2 + 2\alpha_X - \gamma}{2}, \\ L_0 &= 2\frac{A_X}{t_*^{\alpha_X}}\frac{\gamma-1}{2-\gamma}\left(\frac{t_*}{t_q}\right)^k\left(\frac{t_{\rm cut,\ X}}{t_*}\right)^{\frac{2-\gamma}{2}} \\ &= 2A_X\frac{\gamma-1}{2-\gamma}t_q^{-\alpha_X}\left(\frac{t_{\rm cut,\ X}}{t_q}\right)^{\frac{2-\gamma}{2}},\end{aligned} \tag{A14}$$

where we have used Equation (A13). For the present parameters, we obtain $k$=1.219 and $L_0 = 1.011\times10^{47}$ erg s$^{-1}$. Therefore, we can estimate the error of the above quantities as

$$\begin{aligned}\delta k &= \left|\frac{\partial k}{\partial\alpha_X}\right|\delta\alpha_X + \left|\frac{\partial k}{\partial\gamma}\right|\delta\gamma = \delta\alpha_X + \frac{1}{2}\delta\gamma, \\ \delta L_0 &= \left|\frac{\partial L_0}{\partial A_X}\right|\delta A_X + \left|\frac{\partial L_0}{\partial\alpha_X}\right|\delta\alpha_X + \left|\frac{\partial L_0}{\partial\gamma}\right|\delta\gamma \\ &= L_0\left[\frac{\delta A_X}{A_X} + \ln t_q\,\delta\alpha_X + \left|\frac{1}{(\gamma-1)(2-\gamma)}\right.\right. \\ &\quad \left.\left. - \frac{1}{2}\ln\left(\frac{t_{\rm cut,X}}{t_q}\right)\right|\delta\gamma\right],\end{aligned} \tag{A15}$$

which read as $\delta k = 0.170$ and $\delta L_0 \approx 0.792 L_0 \approx 0.801\times10^{47}$ erg s$^{-1}$.

The large uncertainty in the estimate of $t_*$ and $B_{*,0}$ is a consequence of the propagation of the uncertainty of $R_{*,0}$, which arises from the uncertainty in the estimate of the SN time, $t_{\rm SN}$, because it is sensitive to the function of $\Omega_{\nu{\rm NS}}$.

## ORCID iDs

C. L. Fryer https://orcid.org/0000-0003-2624-0056
R. Ruffini https://orcid.org/0000-0003-0829-8318

## References

Amati, L., Frontera, F., Tavani, M., et al. 2002, A&A, 390, 81
Arnett, D. 1996, Supernovae and Nucleosynthesis: An Investigation of the History of Matter from the Big Bang to the Present (Princeton, NJ: Princeton University Press)
Barniol Duran, R., Nakar, E., Piran, T., & Sari, R. 2015, MNRAS, 448, 417
Becerra, L., Bianco, C. L., Fryer, C. L., Rueda, J. A., & Ruffini, R. 2016, ApJ, 833, 107
Becerra, L., Cipolletta, F., Fryer, C. L., Rueda, J. A., & Ruffini, R. 2015, ApJ, 812, 100
Becerra, L., Ellinger, C. L., Fryer, C. L., Rueda, J. A., & Ruffini, R. 2019, ApJ, 871, 14
Becerra, L., Guzzo, M. M., Rossi-Torres, F., et al. 2018, ApJ, 852, 120
Becerra, L. M., Moradi, R., Rueda, J. A., Ruffini, R., & Wang, Y. 2022, PhRvD, 106, 083002
Bianco, C. L., Ruffini, R., & Xue, S.-S. 2001, A&A, 368, 377
Bloom, J. S., Frail, D. A., & Sari, R. 2001, AJ, 121, 2879
Campana, S., Beardmore, A., D'Ai, A., et al. 2017, GCN Circ., 22191, 1
Campana, S., Mangano, V., Blustin, A. J., et al. 2006, Natur, 442, 1008
Chen, W., Xie, W., Lei, W.-H., et al. 2017, ApJ, 849, 119
Cipolletta, F., Cherubini, C., Filippi, S., Rueda, J. A., & Ruffini, R. 2015, PhRvD, 92, 023007
Cipolletta, F., Cherubini, C., Filippi, S., Rueda, J. A., & Ruffini, R. 2017, PhRvD, 96, 024046
Cobb, B. E. 2017, GCN Circ., 22921, 1
Colgate, S. A. 1974, ApJ, 187, 333
Dai, Z. G., & Lu, T. 1998a, A&A, 333, L87

Dai, Z. G., & Lu, T. 1998b, PhRvL, 81, 4301
De Colle, F., Lu, W., Kumar, P., Ramirez-Ruiz, E., & Smoot, G. 2018, MNRAS, 478, 4553
de Ugarte Postigo, A., Izzo, L., Kann, D. A., et al. 2017, GCN Circ., 22204, 1
D'Elia, V., Campana, S., D'Aì, A., et al. 2018, A&A, 619, A66
D'Elia, V., D'Ai, A., Lien, A. Y., & Sbarufatti, B. 2017, GCN Circ., 22177, 1
Eisenberg, M., Gottlieb, O., & Nakar, E. 2022, MNRAS, 517, 582
Fraija, N., Pedreira, A. C. C. d. E. S., & Veres, P. 2019b, ApJ, 871, 200
Fraija, N., Colle, F. D., Veres, P., et al. 2019a, ApJ, 871, 123
Fryer, C. L., Benz, W., & Herant, M. 1996, ApJ, 460, 801
Fryer, C. L., Oliveira, F. G., Rueda, J. A., & Ruffini, R. 2015, PhRvL, 115, 231102
Fryer, C. L., Rueda, J. A., & Ruffini, R. 2014, ApJL, 793, L36
Goldreich, P., & Julian, W. H. 1969, ApJ, 157, 869
Gottlieb, O., Nakar, E., Piran, T., & Hotokezaka, K. 2018, MNRAS, 479, 588
Irwin, C. M., & Chevalier, R. A. 2016, MNRAS, 460, 1680
Izzo, L., Rueda, J. A., & Ruffini, R. 2012, A&A, 548, L5
Izzo, L., Kann, D. A., Fynbo, J. P. U., Levan, A. J., & Tanvir, N. R. 2017a, GCN Circ., 22781, 1
Izzo, L., Selsing, J., Japelj, J., et al. 2017b, GCN Circ., 22180, 1
Izzo, L., de Ugarte Postigo, A., Maeda, K., et al. 2019, Natur, 565, 324
Izzo, L., Auchettl, K., Hjorth, J., et al. 2020, A&A, 639, L11
Kardashev, N. S. 1962, SvA, 6, 317
Kasliwal, M. M., Nakar, E., Singer, L. P., et al. 2017, Sci, 358, 1559
Kathirgamaraju, A., Barniol Duran, R., & Giannios, D. 2016, MNRAS, 461, 1568
Ku, H. H. 1966, JRNBS, 70C, 263
Laskar, T., Hull, C. L. H., & Cortes, P. 2020, ApJ, 895, 64
Lehner, L., Palenzuela, C., Liebling, S. L., Thompson, C., & Hanna, C. 2012, PhRvD, 86, 104035
Leung, J. K., Murphy, T., Ghirlanda, G., et al. 2021, MNRAS, 503, 1847
Li, L., Wu, X.-F., Lei, W.-H., et al. 2018, ApJS, 236, 26
Li, L.-X. 2007, MNRAS, 375, 240
Longair, M. S. 2011, High Energy Astrophysics (Cambridge: Cambridge Univ. Press)
Maity, B., & Chandra, P. 2021, ApJ, 907, 60
Mastrano, A., Lasky, P. D., & Melatos, A. 2013, MNRAS, 434, 1658
Mészáros, P., & Rees, M. J. 2001, ApJL, 556, L37
Metzger, B. D., Giannios, D., Thompson, T. A., Bucciantini, N., & Quataert, E. 2011, MNRAS, 413, 2031
Moradi, R., Rueda, J. A., Ruffini, R., & Wang, Y. 2021a, A&A, 649, A75
Moradi, R., Rueda, J. A., Ruffini, R., et al. 2021b, PhRvD, 104, 063043
Nakar, E. 2015, ApJ, 807, 172
Nakar, E., & Piran, T. 2017, ApJ, 834, 28
Newville, M., Otten, R., Nelson, A., et al. 2021, lmfit/lmfit-py: v1.0.3, Zenodo, doi:10.5281/zenodo.5570790
Pacini, F., & Salvati, M. 1973, ApJ, 186, 249
Pétri, J. 2015, MNRAS, 450, 714
Planck Collaboration, Aghanim, N., Akrami, Y., et al. 2020, A&A, 641, A6
Pons, J. A., & Viganò, D. 2019, LRCA, 5, 3
Ramirez-Ruiz, E., Celotti, A., & Rees, M. J. 2002, MNRAS, 337, 1349
Rastegarnia, F., Moradi, R., Rueda, J. A., et al. 2022, EPJC, 82, 778
Rodríguez Castillo, G. A., Israel, G. L., Tiengo, A., et al. 2016, MNRAS, 456, 4145
Rueda, J. A. 2022, arXiv:2202.00316
Rueda, J. A., & Ruffini, R. 2012, ApJL, 758, L7
Rueda, J. A., & Ruffini, R. 2020, EPJC, 80, 300
Rueda, J. A., Ruffini, R., Karlica, M., Moradi, R., & Wang, Y. 2020, ApJ, 893, 148
Rueda, J. A., Ruffini, R., & Kerr, R. P. 2022a, ApJ, 929, 56
Rueda, J. A., Ruffini, R., Li, L., et al. 2022b, PhRv, 106, 083004
Ruffini, R., Rueda, J. A., Muccino, M., et al. 2016, ApJ, 832, 136
Ruffini, R., Karlica, M., Sahakyan, N., et al. 2018a, ApJ, 869, 101
Ruffini, R., Rodriguez, J., Muccino, M., et al. 2018b, ApJ, 859, 30
Ruffini, R., Wang, Y., Aimuratov, Y., et al. 2018c, ApJ, 852, 53
Ruffini, R., Moradi, R., Rueda, J. A., et al. 2019, ApJ, 886, 82
Ruffini, R., Moradi, R., Rueda, J. A., et al. 2021, MNRAS, 504, 5301
Rybicki, G. B., & Lightman, A. P. 1979, Radiative Processes in Astrophysics (New York: Wiley)
Soderberg, A. M., Kulkarni, S. R., Nakar, E., et al. 2006a, Natur, 442, 1014
Soderberg, A. M., Nakar, E., Berger, E., & Kulkarni, S. R. 2006b, ApJ, 638, 930
Soderberg, A. M., Berger, E., Page, K. L., et al. 2008, Natur, 453, 469
Soker, N. 2022, RAA, 22, 122003
Suzuki, A., & Maeda, K. 2022, ApJ, 925, 148
Suzuki, A., Maeda, K., & Shigeyama, T. 2019, ApJ, 870, 38
Tan, J. C., Matzner, C. D., & McKee, C. F. 2001, ApJ, 551, 946
Tiengo, A., Esposito, P., Mereghetti, S., et al. 2013, Natur, 500, 312
Urata, Y., Toma, K., Huang, K., et al. 2019, ApJL, 884, L58
Vianello, G., Lauer, R. J., Younk, P., et al. 2015, arXiv:1507.08343
Wang, Y., Rueda, J. A., Ruffini, R., et al. 2019, ApJ, 874, 39
Wang, Y., Rueda, J. A., Ruffini, R., et al. 2022, ApJ, 936, 190
Wang, J., Zhu, Z. P., Xu, D., et al. 2018, ApJ, 867, 147
Waxman, E. 2004, ApJ, 602, 886
Wei, J.-B., Figura, A., Burgio, G. F., Chen, H., & Schulze, H. J. 2019, JPhG, 46, 034001
Zhang, B., & Mészáros, P. 2001, ApJL, 552, L35
Zhang, W., Woosley, S. E., & Heger, A. 2004, ApJ, 608, 365
Zhao, L., Liu, L., Gao, H., et al. 2020, ApJ, 896, 42